Hindawi
Journal of Mathematics
Volume 2023, Article ID 9852630, 1 page
https://doi.org/10.1155/2023/9852630

Retraction

Retracted: A New Algorithm for Extracting Winter Wheat Planting Area Based on Ownership Parcel Vector Data and Medium-Resolution Remote Sensing Images

Journal of Mathematics

Received 19 December 2023; Accepted 19 December 2023; Published 20 December 2023

This article has been retracted by Hindawi following an investigation undertaken by the publisher [1]. This investigation has uncovered evidence of one or more of the following indicators of systematic manipulation of the publication process:

(1) Discrepancies in scope

(2) Discrepancies in the description of the research reported

(3) Discrepancies between the availability of data and the research described

(4) Inappropriate citations

(5) Incoherent, meaningless and/or irrelevant content included in the article

(6) Manipulated or compromised peer review

The presence of these indicators undermines our confidence in the integrity of the article's content and we cannot, therefore, vouch for its reliability. Please note that this notice is intended solely to alert readers that the content of this article is unreliable. We have not investigated whether authors were aware of or involved in the systematic manipulation of the publication process.

Wiley and Hindawi regrets that the usual quality checks did not identify these issues before publication and have since put additional measures in place to safeguard research integrity.

We wish to credit our own Research Integrity and Research Publishing teams and anonymous and named external researchers and research integrity experts for contributing to this investigation.

The corresponding author, as the representative of all authors, has been given the opportunity to register their agreement or disagreement to this retraction. We have kept a record of any response received.

References

[1] H. Xie, Q. Wu, T. Zhang et al., "A New Algorithm for Extracting Winter Wheat Planting Area Based on Ownership Parcel Vector Data and Medium-Resolution Remote Sensing Images," *Journal of Mathematics*, vol. 2021, Article ID 1860160, 16 pages, 2021.

Hindawi
Journal of Mathematics
Volume 2021, Article ID 1860160, 16 pages
https://doi.org/10.1155/2021/1860160

Research Article

A New Algorithm for Extracting Winter Wheat Planting Area Based on Ownership Parcel Vector Data and Medium-Resolution Remote Sensing Images

Huaming Xie,[1,2] Qianjiao Wu ,[2,3] Ting Zhang,[1,2] Zhende Teng,[1] Hao Huang,[1,2] Ying Shu,[1,2] Shaoru Feng,[1,2] and Jing Lou[4]

[1]*School of Environment and Energy Engineering, Anhui Jianzhu University, Hefei 230601, China*
[2]*Institute of Remote Sensing and Geographic Information Systems, Anhui Jianzhu University, Hefei 230601, China*
[3]*School of Public Policy & Management, Anhui Jianzhu University, Hefei 230601, China*
[4]*Remote Sensing Application Center, Ministry of Agriculture, Hefei Branch, Hefei 230601, China*

Correspondence should be addressed to Qianjiao Wu; qianjiaowu@ahjzu.edu.cn

Received 29 October 2021; Revised 22 November 2021; Accepted 24 November 2021; Published 14 December 2021

Academic Editor: Naeem Jan

In the complex planting area with scattered parcels, combining the parcel vector data with remote sensing images to extract the winter wheat planting information can make up for the deficiency of the classification from remote sensing images simply. It is a feasible direction for precision agricultural subsidies, but it is difficult to collect large-scale parcel data and obtain high spatial resolution or time-series remote sensing images in mass production. It is a beneficial exploration of making use of existing parcel data generated by the ground survey and medium-resolution remote sensing images with suitable time and spatial resolution to extract winter wheat planting areas for large-scale precision agricultural subsidies. Therefore, this paper proposes a new algorithm to extract winter wheat planting areas based on ownership parcel data and medium-resolution remote sensing images for improving classification accuracy. Initially, the segmentation of the image is carried out. To this end, the parcel data is used to generate the region of interest (ROI) of each parcel. Second, the homogeneity of each ROI is detected by its statistical indices (mean value and standard deviation). Third, the parallelepiped classifier and rule-based feature extraction classification methods are utilized to conduct the homogeneous and nonhomogeneous ROIs. Finally, two classification results are combined as the final classification result. The new algorithm was applied to a complex planting area of 103.60 km^2 in central China based on the ownership parcel data and Gaofen-1 PMS and WFV remote sensing images in this paper. The experimental results show that the new algorithm can effectively extract winter wheat planting area, eliminate the problem of salt-and-pepper noise, and obtain high-precision classification results (kappa = 0.9279, overall accuracy = 96.41%, user's accuracy = 99.16%, producer's accuracy = 93.39%, commission errors = 0.84%, and omission errors = 6.61%) when the size of ownership parcels matches the spatial resolution of remote sensing images.

1. Introduction

Accurate extraction of crop planting structure is fundamental to understanding the information of crop growth and yield and agricultural disasters, which have great value in formulating national agricultural policies and guaranteeing national food security [1–3]. With controllable costs, obtaining accurate crop planting areas of small peasant households for every season through remote sensing and geographic information technology is important to improve the precision and directivity of agricultural planting subsidies in the complex planting area [4].

There are numerous approaches for extracting crop planting areas using advanced remote sensing images from multiple sensors [5–10]. These approaches can be categorized as pixel-based, object-based, or a combination of the two [11]. Pixel-based methods consist of maximum likelihood classification [12–14], spectral angle mapper [15, 16], random forest classifier [17–20], support vector machine [21–23], tassel cap brightness–greenness–wetness [24, 25],

decision tree algorithm [26, 27], phenological algorithm [28–30], and machine learning algorithm [31–33]. Object-based methods include hierarchical image segmentation software [11, 34, 35] and rule-based feature extraction [36, 37]. Combining methods using object-based and pixel-based methods has been proposed to classify crops planting areas [38–40]. However, these methods are difficult to achieve breakthroughs in automatic classification and visual recognition of crop planting areas simply from the spectral information of remote sensing images in the scattered and small planting areas [41–44]. Combining the parcel data with remote sensing image to extract the structure information of crop planting can make up for the deficiency of the classification from remote sensing images simply and obtain better classification accuracy. It provides a simple and effective method to resolve the problems of spectral variation and spectral mixing in pixel-based classification methods and is a feasible direction for remote sensing of large-scale precision agricultural subsidies [45–49].

The idea of parcel-based crop planting classification originated by Derenyi [50], which is still a research hotspot in the field of remote sensing information extraction of crop planting. Recently, parcel-based crop planting classification research has focused on parcels obtained by vectorization or image segmentation [51–54]. Previous studies on parcel-based classification usually use digitization or image segmentation to extract the parcel data and use multispectral images or time-series images to carry out the crop planting classification with a variety of classifiers. It is difficult to collect large-scale parcel data. Moreover, incorporating high spatial resolution or time-series remote sensing images and parcel data is difficult to obtain remote sensing image in mass production and is not conducive to promotion and application. Recently, confirming and registering the contracted management rights of rural land in China have accumulated an amount of ownership parcel data, which provide an ideal data source for the parcel-based classification methods. It is a beneficial exploration of making use of existing parcel data generated by the ground survey and medium-resolution remote sensing images with suitable time and spatial resolution to extract crop planting information for large-scale precision agricultural subsidies [53–56].

Moreover, remote sensing images with different spatial resolutions have their own applicability and limitations in the crop planting classification [57, 58]. Remote sensing images with low spatial resolution have high temporal resolution and can cover a large region, but limited by the spatial resolution, there are many mixed pixels, and they can only be applied to extract crop planting areas roughly. Remote sensing images with high spatial resolution provide more abundant information about structure, texture, and geometry but generally have a low temporal resolution, making it challenging to obtain key phenological period images of different crops. In addition, using them multiplies the workload of data processing. Remote sensing images with medium spatial resolution have better accuracy and target recognition reliability. However, applied to mountains, hills, and other complex terrain regions with numerous mixed pixels, crop planting structures are insufficiently expressed and have low interpretation accuracy. It is possible to overcome this shortcoming if we combine the vector boundary information of the parcel with medium spatial resolution remote sensing images to extract crop planting areas.

Therefore, this study proposes a new algorithm for extracting winter wheat planting areas based on ownership parcel vector data and medium-resolution remote sensing images to improve the extraction accuracy. To verify its feasibility, accuracy, and applicability, the new algorithm was applied to a complex planting area of 103.60 km^2 in central China in 2018. Moreover, the matching relationship between the size of parcels and the spatial resolution of remote sensing images was discussed in this paper.

The paper is organized as follows: Section 2 describes the study area and data. The methods are presented in Section 3. The experimental results and discussion are given in Section 4. Section 5 concludes the paper and indicates directions for further research.

2. Materials and Methods

In this section, the methodology of the study and essential tools are elaborated.

2.1. Study Area. We selected a complex planting area of 103.60 km^2 in central China as the study area. The study area covers the 19 administrative villages of Fengle Town, in Feixi County, Hefei City, Anhui Province, China. It extends from 31°32′34.77″ to 31°39′29″ N and 117°2′10″ to 117°12′23″ E. The area's terrain is relatively flat, with a general trend of being lower from north to south. It is in a subtropical monsoon climate zone with the characteristics of remarkable monsoon climate, mild climate, moderate rainfall with an annual average of 1020.6 mm, adequate light, and a long frost-free period. It had a total population of 45,726 in 2017. The study area was registered as arable land with a total area of 6317.95 hectares in 2018. Because it is near the capital city of Anhui Province, there are more economic agricultural crops in the region. Production mainly uses small agricultural machinery and artificial operation modes. The structure of crop planting is more complex in the region, which is distributed in a scattered and discontinuous mode. Wheat, rice, and other food products are the main crops in this region, accounting for about 70% of the total crop planting area. There are also other crops, such as rape, cotton, vegetables, melons, and fruits. It is a typical region with a hilly landform and complex planting structure in the Yangtze River delta region. Extracting the winter wheat planting area in this region has certain representativeness and typicality by combining vector boundaries of ownership parcels and remote sensing images. Figure 1 displays the map of study area.

2.2. Data Processing. The components of data processing are described in this section.

2.2.1. Ownership Parcel Data. In January 2015, the Chinese Ministry of Agriculture, Ministry of Finance, and four other departments jointly issued their "opinions on earnestly

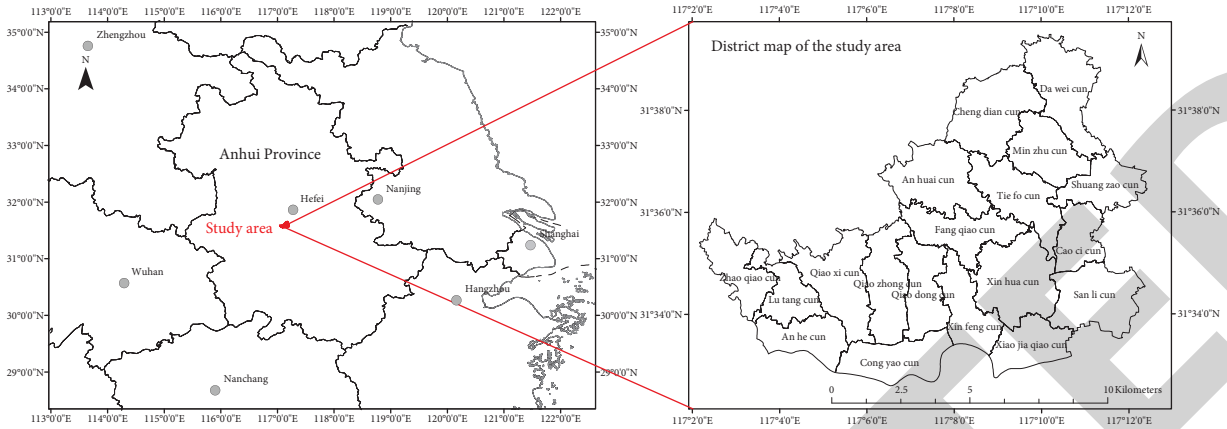

Figure 1: Location map of the study area.

confirming, registering, and certifying the contracted management rights of rural land" and required that the following be completed by the end of 2017: (1) carrying out a comprehensive inventory of land contract files and materials to find out the status of contracted fields; (2) mastering the situation of contracted peasant households, checking contractor representatives and family members, and collecting their changes and other information; and (3) investigating contracted field management rights to find out the ownership rights of contracted fields. The survey of contracted field status completed the geospatial information of all agricultural planting parcels and the corresponding contractor information. The survey of geospatial information and corresponding contractor information for all agricultural parcels was completed to investigate contracted field status. Figure 2 illustrates the ownership parcel map of the study area.

The land contractual management rights confirmation and registration database of the study area was collected from the Agriculture and Rural Affairs Bureau of Feixi County on December 31, 2017. Aerial remote sensing orthophoto images with 0.5 m spatial resolution were obtained at the end of 2017 and were matched with the collected data, as shown in Figure 2. This database contains class files of parcel elements and an attribute table of contracted parcels in shape (shp) format, the information of contractors in the table and access library, and other information. A unified query of "parcel code" and "contractor code" fields can obtain the spatial vector positions of all parcels and the ownership information of contracted farmers. The spatial vector and ownership information can be derived from the database. There was a total of 71,869 parcels, among which the minimum area was 10.98 m^2, the maximum area was 21,604.77 m^2, the average area was 879.09 m^2, and the standard deviation of the area was 850.37.

2.2.2. Medium Spatial Resolution Remote Sensing Images. We selected Gaofen-1 satellite panchromatic multispectral sensor (PMS) images with a spatial resolution of 8 meters from March 11, 2018, and wide field view (WFV) images with a spatial resolution of 16 meters from February 23, 2018. They are shown in Figure 3.

The Gaofen-1 satellite carries two 2 m panchromatic and 8 m multispectral cameras and four 16 m multispectral cameras. The sensor parameter information is shown in Table 1. PMS and WFV have four bands: red, green, blue, and near-infrared. The spectral reflectance of the green and near-infrared bands is sensitive to winter crops and can be beneficial in effectively identifying winter wheat. Images with 8 m and 16 m resolution are typical medium-resolution images, commonly applied to extract the structure information of winter wheat plantings in large regions.

We selected the most recognizable growing period of winter wheat in the Jianghuai region from February to March for the time phase of remote sensing images. In this region, winter wheat is sown in early November and harvested in mid-June. The seedling stage is from mid-December to mid-January. From early February to early April, the winter wheat returns to green for the jointing and heading stages. This is the time when it is the easiest to differentiate winter wheat in remote sensing images.

Gaofen-1 satellite images can be downloaded from the China Resources Satellite Ground Application Center (http://36.112.130.153:7777/DSSPlatform/index.html) for free. The data preprocessing of the two images included the following:

(i) Orthorectifying RPC points combined with 30 m DEM

(ii) Converting the coordinate system from the WGS-84 geographic coordinate system (GCS_WGS_1984) to the CGCS2000 geodetic coordinate system with a 3-degree Gaussian kriging projection coordinate system under a central longitude of 117′ E (CGCS2000_3_Degree_GK_CM_117E)

(iii) Utilizing accurately calibrated aerial remote sensing orthophoto images with 0.5 m spatial resolution, whose coordinate system is also CGCS2000_3_Degree_GK_CM_117E, to perform geometric precision correction of PMS and WFV images in order to keep the local error to less than 2 pixels and the average error less than 1 pixel

(iv) Clipping the two remote sensing images using the vector administrative region data of the study area

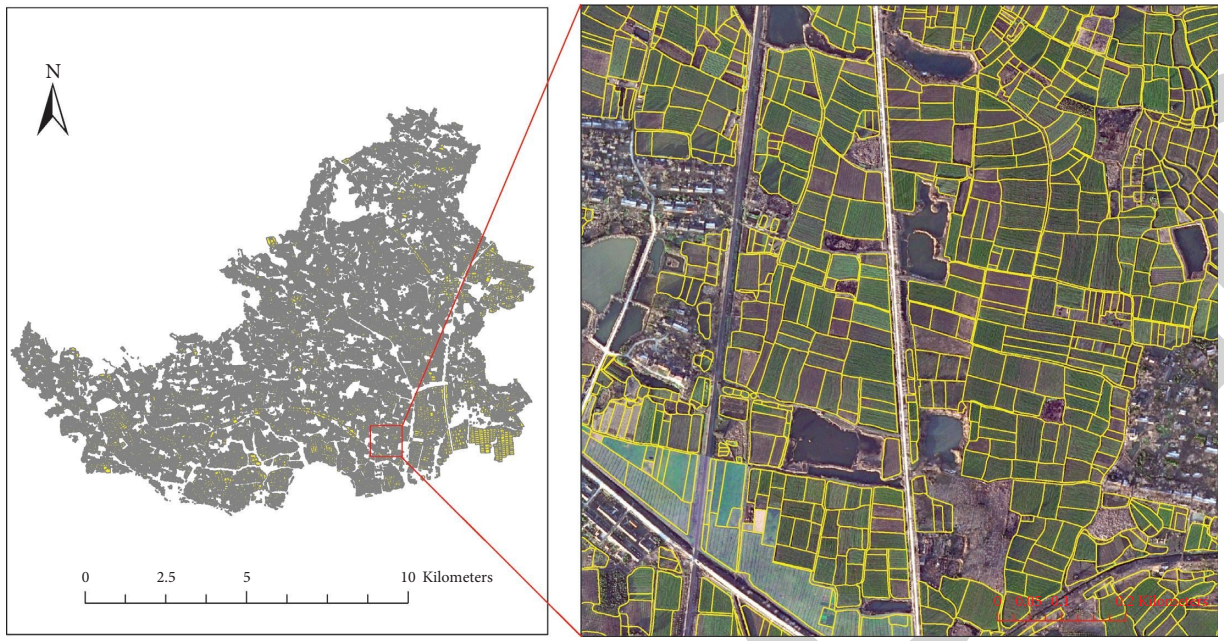

Figure 2: Ownership parcel data of the study area.

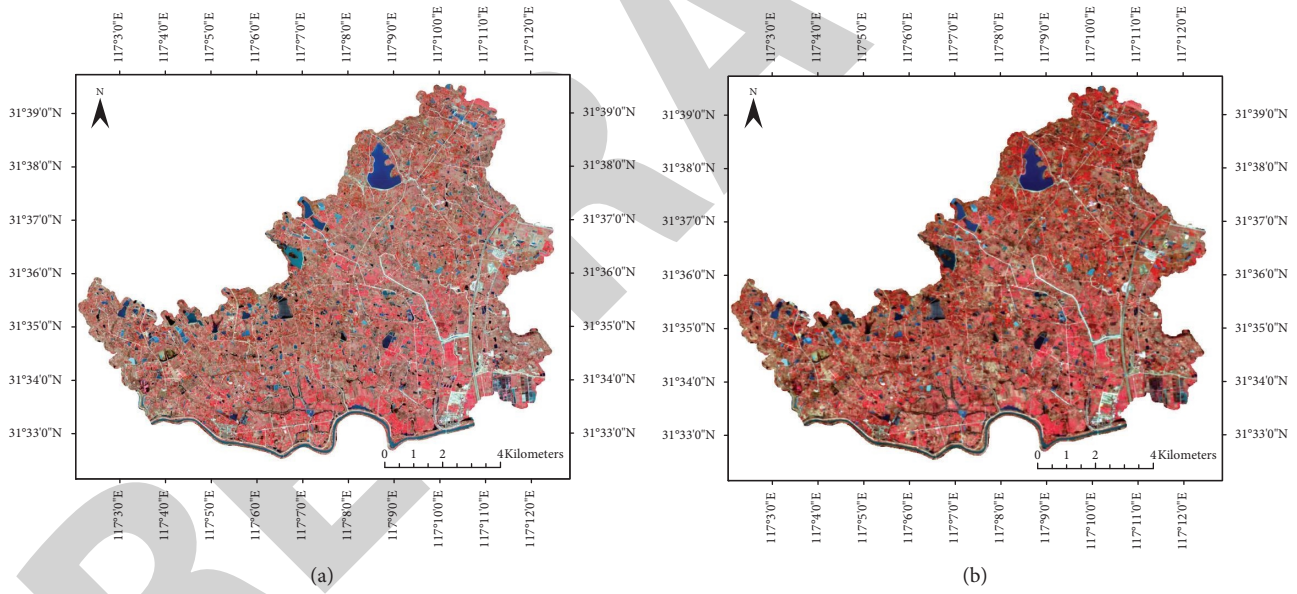

Figure 3: Remote sensing satellite images selected in this paper: (a) Gaofen-1 (GF-1) satellite PMS image with 8 m spatial resolution. (b) GF-1 satellite WFV image with 16 m spatial resolution.

Table 1: Sensor parameter information of Gaofen-1 satellite PMS and WFV images.

	Spectrum (μm)	Spectrum range	Spatial resolution (m)	Breadth (km)	Swinging ability	Revisit time (days)
Panchromatic multispectral camera	1	0.45~0.90	2	60 (two combination cameras)	±35°	4
	2	0.45~0.52	8			
	3	0.52~0.59				
	4	0.63~0.69				
	5	0.77~0.89				
Multispectral camera	6	0.45~0.52	16	800 (four combination cameras)		2
	7	0.52~0.59				
	8	0.63~0.69				
	9	0.77~0.89				

2.2.3. Sample Data of Crop Planting Conditions. There were 1,038 parcels or nonagricultural cropping samples for spring crop plantings in 2018 by field investigation. These parcels include 524 samples of winter wheat and 514 samples of other crops, noncrops, and noncrop nonagricultural plantings. There were 253 winter wheat samples used for information extraction of remote sensing images and 271 winter wheat samples for accuracy verification. There were 240 samples of other crops or noncrops used for classification and 274 samples for accuracy verification. The statistical data are shown in Table 2.

2.2.4. Relationship between the Size of Parcels and Spatial Resolution of Remote Sensing Images. There are some differences between the ownership parcel of small peasant households and those parcels obtained by vectorization or image segmentation. If the area of ownership parcels is small, there are the same crops of one season planted in the ownership parcels basically. The overall distribution of the size of parcels also affects the optimal spatial resolution of remote sensing images, because there should be enough pixels in the parcel. Thus, the optimal matching relationship between them needs to be further discussed.

There is a certain matching relationship between the size of parcels and the spatial resolution of remote sensing images. In general, if a parcel has purer pixels except for the boundary pixels, it is beneficial to classify different crops. However, if the parcel area is too large, it may have mixed cropping; there will be multiple crops within the parcel, which is not conducive to the winter wheat classification.

As shown in Figure 4 and Table 3, parcels of 200–500, 500–1,000, and 1,000–1,500 m^2 in the study area accounted for 28.82, 33.08, and 15.92%, respectively. Parcels with less than 1,500 m^2 accounted for 86.04%. This demonstrates that the parcels in this region were generally small and fragmented.

From Table 3, we can see that, for GF-PMS images, parcels with an area less than 200 m^2, accounting for 8.22% of the total, have a large majority of mixed pixels. Parcels with an area of 200–500 m^2, accounting for 28.82% of the total, have more mixed pixels. Parcels with an area of 500–3,500 m^2, accounting for 61.46% of the total, have purer pixels, and the pixels are relatively appropriate in these parcels.

For GF-WFV images, parcels with an area less than 1,000 m^2, accounting for 70.12% of the total, have a large majority of mixed pixels, which is not conducive to classification. Parcels with an area of 1,000–1,500 m^2, accounting for 15.92% of the total, have more mixed pixels. Parcels with an area of 1,500–3,500 m^2, accounting for 12.46% of the total, have purer pixels, and the pixels are appropriate to the parcels. For the two images, parcels with an area of more than 3,500 m^2, accounting for 1.50% of the total, have large areas and may be planted with mixed crops.

In theory, the GF-PMS (8 m) remote sensing image has a higher matching degree with the size of parcels in the study area, and the classification accuracy should be higher. The GF-WFV (16 m) image has a relatively low matching degree, which cannot reflect the advantages of combination classification. These are further validated later.

3. Methods

This research aimed to utilize ownership parcel data and medium spatial resolution remote sensing images to classify the winter wheat in the complex planting area accurately. The methodology adopted for this paper had 6 parts: (1) building the region of interest (ROI) to obtain the statistical indices; (2) detecting and determining the homogeneity of each ROI; (3) classifying the winter wheat within the homogeneous ROIs; (4) classifying the winter wheat within the nonhomogeneous ROIs; (5) selecting comparison classification methods; and (6) evaluating the classification accuracy. The specific steps of the combination classification are illustrated in Figure 5. IDL language and Envi software were implemented for coding and data processing.

3.1. Building the Region of Interest (ROI) to Obtain Statistical Indices. Due to the abundant spectral and textural features of different crops in remote sensing satellite images, these features are typically explored to design statistical indices to monitor winter wheat classes. However, classification results based on remote sensing images cannot focus on the ownership and management of crop planting regions. The ownership parcel data can make up for this deficiency.

Therefore, the ownership parcels were combined with the remote sensing images to build the regions of interest (ROIs), which have the spectral and textural features of the remote sensing images and all of the information of the ownership parcels. The remote sensing images were logically segmented by the ownership parcels, and a corresponding ROI was obtained for each parcel. The statistical indices of each ROI were extracted from the band spectrum digital number (DN) value of its corresponding remote sensing images and written into the attribute table of parcels. The statistical indices express the mean value and standard deviation of the DN values.

3.2. Detecting and Determining the Homogeneity of Each ROI. In general, the same crops may be planted in ROIs with a small area and belong to the same ownership contractor. There may be different crops planted in ROIs with a large area or in special cases. Thus, it is essential to detect whether the same crop is the winter wheat planted in the ROI. If it is determined that the same crop is planted, it can be considered in its entirety to judge whether it is the winter wheat. Otherwise, it is necessary to classify different crops to extract the planting area of the winter wheat.

Generally speaking, if the crop type of the ROI is consistent, its spectral value should be basically consistent. Therefore, it can be detected by the standard deviation of the spectral value. If the standard deviation of the spectral value of the ROI to be detected is less than K times the standard deviation of the sample, both the crop type and ROI are considered to be homogeneous. Otherwise, the parcel is regarded as a nonhomogeneous ROI. The detection formula is as follows:

Table 2: Statistical data for samples of crop planting conditions.

	Winter wheat (parcels)	Others (parcels or region)	Total
Classification samples	253	240	493
Accuracy verification samples	271	274	545
Total	524	240	1,038

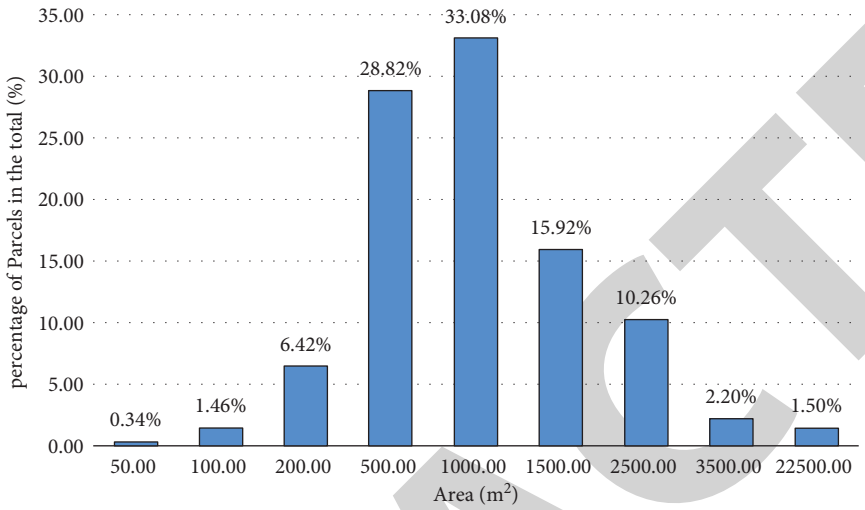

Figure 4: Histogram of the proportion of areas of ownership parcels.

Table 3: Matching between the area of ownership parcels and GF-PMS and GF-WFV images.

Parcel area (m^2)	Parcel number	Proportion (%)	GF-PMS (8 m) Parcel number	GF-PMS (8 m) Applicable situation	GF-PMS (8 m) Proportion sum (%)	GF-WFV (16 m) Parcel number	GF-WFV (16 m) Applicable situation	GF-WFV (16 m) Proportion sum (%)
0~50	241	0.34	1	Large majority of mixed pixels	8.22	1	Large majority of mixed pixels	70.12
50~100	1,052	1.46	1-2			1		
100~200	4,616	6.42	2–4			1		
200~500	20,715	28.82	4–8	More mixed pixels	28.82	1-2		
500~1,000	23,771	33.08	8–16			2–4		
1,000~1,500	11,443	15.92	16–24	More pure pixels (number of pixels in parcel is appropriate)	61.46	4–6	More mixed pixels	15.92
1,500~2,500	7,373	10.26	24–40			6–10	More pure pixels (number of pixels in parcel is appropriate)	12.46
2,500~3,500	1,583	2.20	40–55			10–14		
>3,500	1,075	1.50	55–352	Large area (there may be mixed crops)	1.50	14–88	Large area (there may be mixed crops)	1.50
Total	71,869	100	—	—	100	—	—	100

$$\left\{\begin{array}{l} B1i_{\text{stdDev}} \le K * B1s_{\text{stdDev}} \\ B2i_{\text{stdDev}} \le K * B2s_{\text{stdDev}} \\ B3i_{\text{stdDev}} \le K * B3s_{\text{stdDev}} \\ B4i_{\text{stdDev}} \le K * B4s_{\text{stdDev}} \end{array}\right\}, \quad (1)$$

where $B1i_{\text{stdDev}}$ denotes the standard deviation of band 1 for the ith ROI, $B1s_{\text{stdDev}}$ denotes the standard deviation of band 1 for the sample, and K denotes the threshold value of detecting the homogeneity of the ROI, regarded as a coefficient, which depends on the actual situation.

Because different ground features have different standard deviations, it is difficult to use a series of threshold values to examine the homogeneity of all ground features. A series of threshold values can only examine the homogeneity of one type of ground feature. In this paper, the threshold value of detecting the homogeneity of ROIs for GF-PMS and GF-WFV images was obtained by using K times the standard deviation of the classified samples, and K was tried with two numbers, 1.5 and 2. The detailed information is shown in Table 4.

3.3. Classifying the Winter Wheat within the Homogeneous ROIs. For homogeneous ROIs, it is only necessary to determine whether the planted crop is winter wheat. The parallelepiped classifier is utilized to classify the winter wheat for homogeneous ROIs in this paper. It calculates the mean value of each band of the ROI to be classified and then judges whether it is within the range of K times the mean value of the

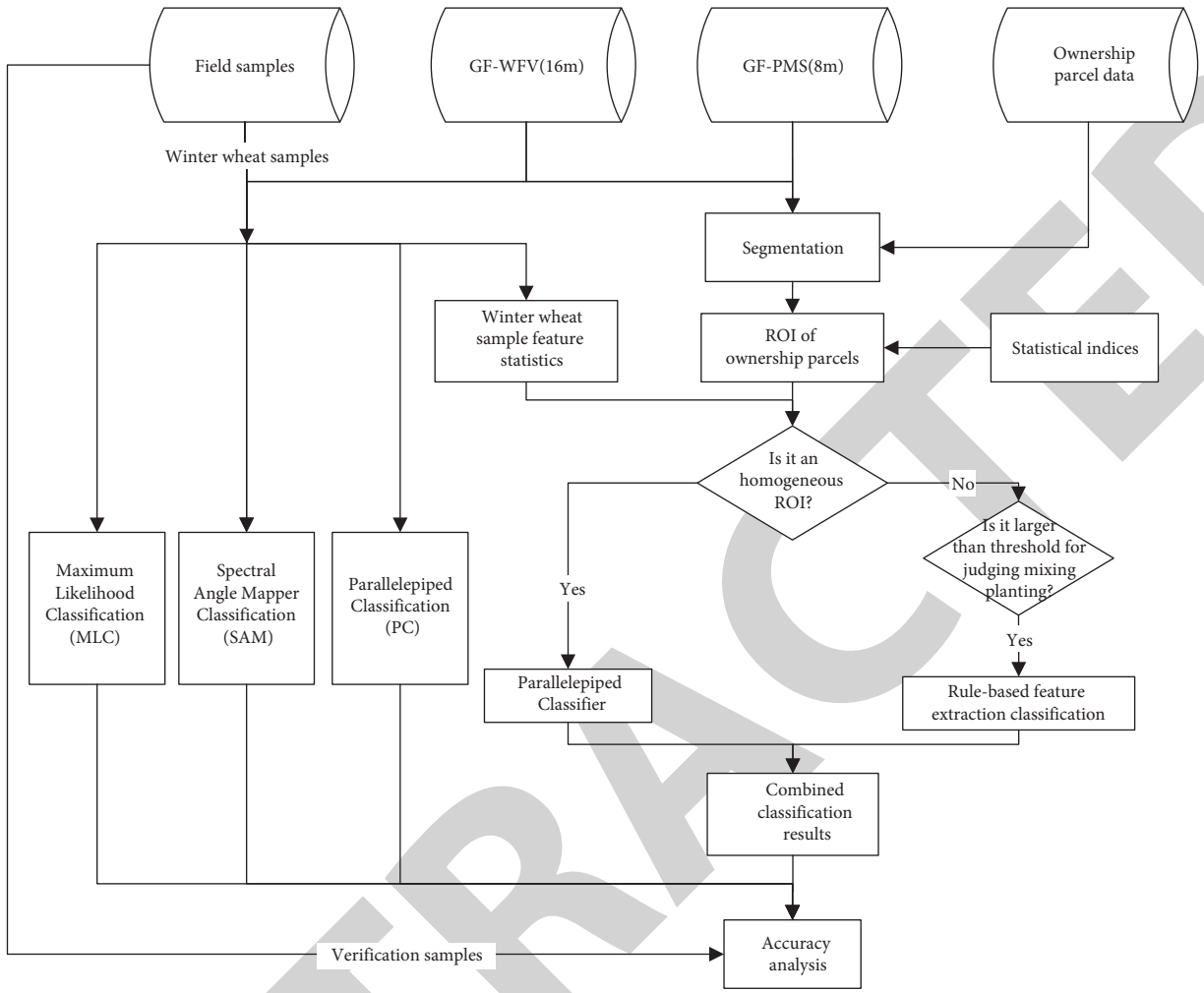

Figure 5: Flowchart of the new algorithm for extracting winter wheat planting area in this paper.

Table 4: Threshold of detecting homogeneity of ROIs for GF-PMS and GF-WFV images.

Band	Sample for GF-PMS		Threshold value	Sample for GF-WFV		Threshold value
	Mean	Std. dev.		Mean	Std. dev.	
B1 (blue)	387.87	16.28	ROUNDUP[2] (K ∗ 16.28, 0)	275.27	9.71	ROUNDUP (K ∗ 9.71, 0)
B2 (green)	378.81	24.53	ROUNDUP (K ∗ 24.53, 0)	252.90	16.83	ROUNDUP (K ∗ 16.8, 0)
B3 (red)	254.94	28.46	ROUNDUP (K ∗ 28.46, 0)	220.35	20.08	ROUNDUP (K ∗ 20.08, 0)
B4 (near-infrared)	553.54	69.87	ROUNDUP (K ∗ 28.46, 0)	339.84	37.91	ROUNDUP (K ∗ 37.91,0)

ROUNDUP (n, 0) indicates rounding up and keeping 0 decimal places.

standard deviation of the crop sample, shown as equation (2). If the mean value of all bands for the ROI is within the preset range, it is regarded as a homogeneous ROI.

$$\left\{\begin{array}{l} B1s_{\text{mean}} - K * \text{stdDev} \le B1i_{\text{mean}} \le B1s_{\text{mean}} + K * \text{stdDev} \\ B2s_{\text{mean}} - K * \text{stdDev} \le B2i_{\text{mean}} \le B2s_{\text{mean}} + K * \text{stdDev} \\ B3s_{\text{mean}} - K * \text{stdDev} \le B3i_{\text{mean}} \le B3s_{\text{mean}} + K * \text{stdDev} \\ B4s_{\text{mean}} - K * \text{stdDev} \le B4i_{\text{mean}} \le B4s_{\text{mean}} + K * \text{stdDev} \end{array}\right\}, \quad (2)$$

where $B1i_{\text{mean}}$ denotes the mean value of the standard deviation of band 1 for the ith parcel, $B1s_{\text{mean}}$ denotes the mean value of the standard deviation of band 1 for the sample, and K denotes the threshold for detecting the homogeneity of the ROI.

Figure 6 shows the spectral curves of the maximum value, sum of mean value and standard value, mean value, the difference between the mean value and standard value, and minimum value of the four bands of the samples for GF-PMS and GF-WFV images. It can be seen that the standard deviation is not large, although the maximum and minimum values of the wheat samples vary greatly in each band. The values of each pixel in the ROI are close to the mean value, so it is feasible to use the parallelepiped classifier to process homogeneous ROIs for the winter wheat classification.

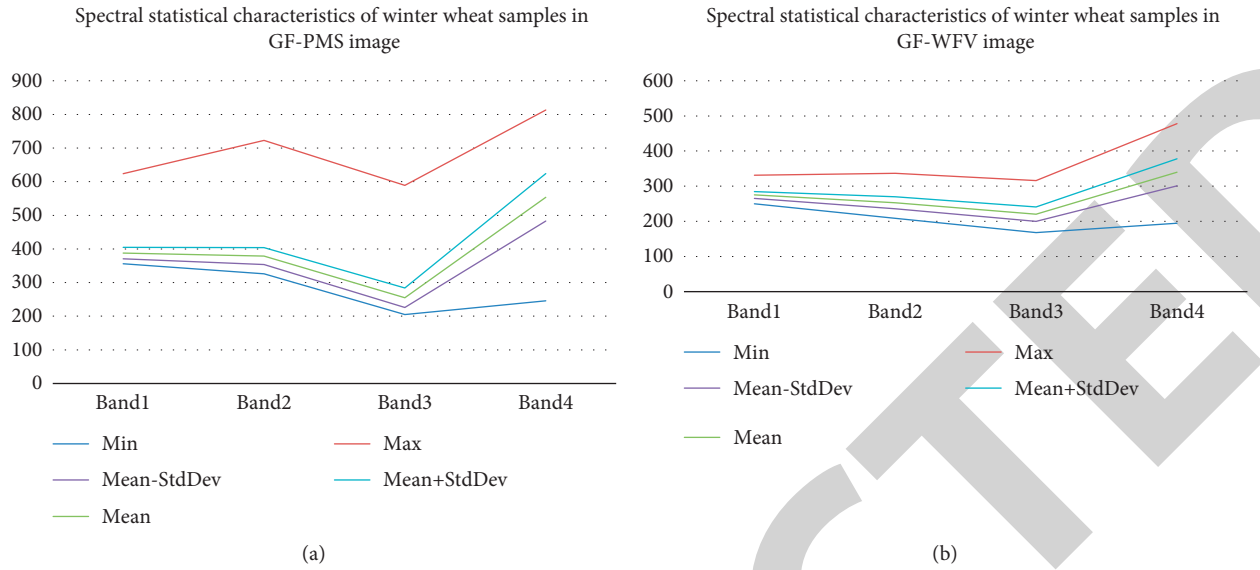

Figure 6: Statistical indices of various spectral bands of remote sensing images of winter wheat sample region: (a) GF1 PMS image; (b) GF1 WFV image.

3.4. Classifying the Winter Wheat within the Nonhomogeneous ROIs. Nonhomogeneous ROIs indicate that the planting area cannot be planted with the same crop. There are two cases to be discussed in this context. One case is that the area of the ROI is smaller than the threshold value (S_t) for judging mixing planting. There is a low probability of mixing planting, and it is directly judged like the other crops. The other case is that the area of the ROI is larger than the threshold value (S_t) for judging mixing planting. The ROI may be planted with different crops, and it is necessary to regard it as an independent image for pixel-based classification. The rule-based feature extraction classification method is adopted to deal with nonhomogeneous ROIs in this paper. Finally, the classification results for homogeneous and nonhomogeneous ROIs are combined as the final classification result. The threshold value for judging mixing planting (S_t) is used as the parameter and input in the specific operation.

In the study area of this paper, S_t is 3500 m^2 which has been analyzed through Section 2.3.2. The rule-based feature extraction method directly invokes the ENVI_FX_RULE-BASED_DOIT module in Envi ver. 5.3. The rule file is defined by the range of K times of the standard deviation of the mean value of the spectral value from winter wheat samples, similar to equation (2), which judges the mean value of the spectrum of the ROI, while it also judges every pixel in the ROI.

3.5. Selecting Comparison Classification Methods. In order to compare the accuracy of the new algorithm, this study selected the maximum likelihood classification (MLC), spectral angle mapper (SAM) classification, and parallelepiped classification (PC) methods for the GF-PMS and GF-WFV images in the study area. Different combinations of input parameters were also adopted for each method, as shown in Table 5.

3.6. Evaluating the New Algorithm's Crop Planting Classification Accuracy. The stratified sampling method was employed to evaluate the new algorithm's crop planting classification accuracy. A total of 271 samples of wheat planting parcels and 274 samples of other ground features were used to verify the accuracy in this study. The kappa, overall accuracy, user's accuracy, producer's accuracy, and commission and omission errors [59, 60] were calculated from the established error matrix of each classification method.

Because the 253 classified wheat samples could comprehensively cover the actual surface state of wheat parcels, it was difficult for the 240 other samples to fully cover images on the entire actual surface state of non-wheat parcels due to their numerous actual feature states, and in the accuracy evaluation, the unclassified category in the classification results is also classified as "other" before the accuracy evaluation.

4. Results and Discussion

The entire study area in this research is 103.60 km^2 and the total area of the ownership parcels is 6317.95 hectares. According to the statistics from the agricultural department, the sowing area of winter wheat in the spring of 2018 was 1226.90 hectares. This was approximated by the proportion of winter wheat acreage planted in several sampled small regions and is regarded as the reference area.

Field survey samples were used to classify GF-PMS and GF-WFV images in the study area using the four methods with ten parameters. Figures 7 and 8 show the best classification results on the GF-PMS and GF-WFV images for each method. The classification accuracy and planting areas of winter wheat from different classification methods were calculated and are shown in Table 6.

Table 5: Threshold of detecting homogeneity of ROIs for GF-PMS and GF-WFV images.

Classification method	Corresponding parameters
Maximum likelihood classification (MLC)	Probability threshold 0.8 (single value)
	Probability threshold 0.9 (single value)
Spectral angle mapper (SAM) classification	Maximum angle 0.1 (single value)
	Maximum angle 0.15 (single value)
Parallelepiped classification (PC)	Max std. dev. from mean 1.5 (single value)
	Max std. dev. from mean 2 (single value)
	Max std. dev. from mean 1.5, 0 (multiple value: 1.5 for wheat, 0 for others)
	Max std. dev. from mean 2, 0 (multiple value: 2 for wheat, 0 for others)
New algorithm	$K = 1.5$; $S_t = 3500\,m^2$
	$K = 2.0$; $S_t = 3500\,m^2$

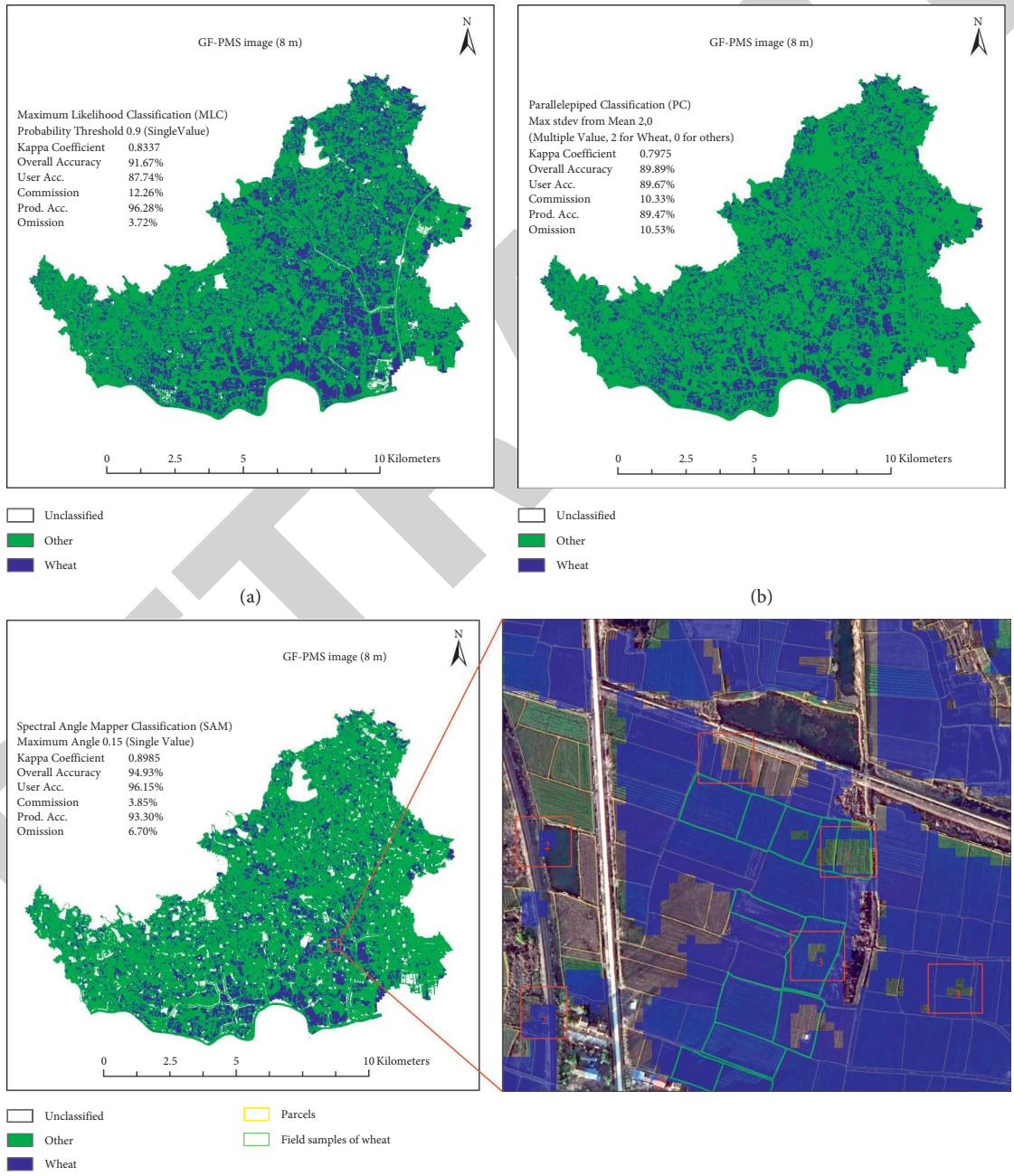

Figure 7: Continued.

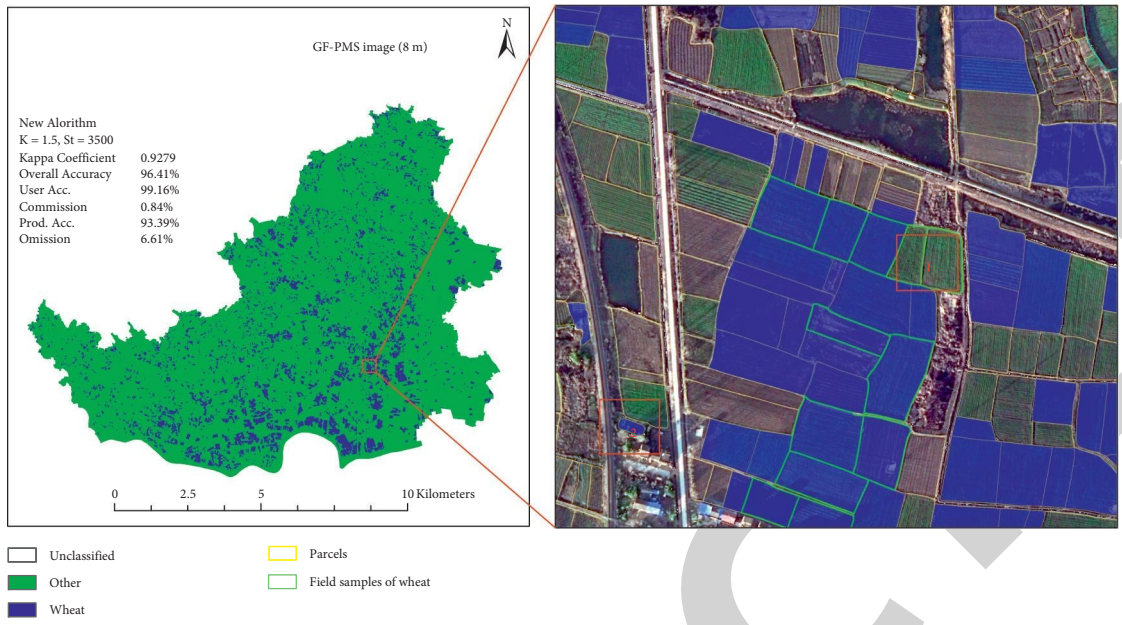

(d)

Figure 7: Best classification results on GF-PMS images in the study area from different methods. (a) MLC. (b) PC. (c) SAM. (d) New algorithm.

4.1. Accuracy Analysis. This section explains the accuracy of the results and carries out an analysis of the matter.

4.1.1. Overall Accuracy of Classification Results. From Table 6, we know that the winter wheat planting area varied greatly among the different methods. Taking the GF-PMS image as an example, according to the MLC, SAM, PC, and new methods, the winter wheat planting area reached 3063.60, 1812.13, 2406.76, and 1018.77 hectares, respectively, showing a threefold difference between them.

There are also significant differences in accuracy between the four classification methods under different parameters from Table 6. On the GF-PMS image, the accuracy of the new algorithm was the highest with K of 1.5 and kappa coefficient, overall accuracy, user's accuracy, commission error, producer's accuracy, and omission error of 0.9279, 96.41%, 99.16%, 0.84%, 93.39%, and 6.61%, respectively. For the PC method, the best classification accuracy was with kappa coefficient, overall accuracy, user's accuracy, commission error, producer's accuracy, and omission error of 0.7975, 89.89%, 89.67%, 10.33%, 89.47%, and 10.53%, respectively, showing a difference from the new method. The worst classification accuracy for the PC method was with kappa coefficient, overall accuracy, user's accuracy, commission error, producer's accuracy, and omission error of 0.2636, 63.98%, 99.91%, 0.09%, 25.83%, and 74.17%, respectively.

It should be noted that a small difference in accuracy can result in a large difference in detecting the winter wheat planting area. Taking the GF-PMS image as an example, the classification results with the highest accuracy detected a wheat planting area of 1028.77 hectares and the classification results with second-highest accuracy detected 1812.13 hectares. This difference is nearly double. It can be seen that, in regions with complex sporadic planting, different parameters in the classification methods have a significant impact on the results. What seems like good classification accuracy could turn out to be extremely different from the actual situation.

4.1.2. Comparative Analysis with the Traditional Classification Method. The study selected the best classification results from the other methods to compare the results from Table 6. We can see that the MLC method has lower accuracy than the new algorithm. The area extracted from the GF-PMS and GF-WFV images is about 3,063 and 4,015.56 hectares, respectively, which are much larger than the reference area (1226.90 hectares). Figures 7(a) and 8(a) also indicate that the MLC method tends to overidentify winter wheat and has a higher commission error, which may be caused by the underrepresentation of classification samples from other categories. The parallelepiped classification method has lower accuracy than the proposed algorithm, but the area it extracted (1,194.73 hectares) is closer to the reference area on the GF-PMS image. In addition, the parallelepiped classification method has high omission and low commission error.

Although the SAM method has the highest accuracy among the algorithms on the two images, the kappa coefficient, overall accuracy, user's accuracy, and producer's accuracy are lower than those of the new algorithm, and the omission and commission errors are higher on the GF-PMS image. Compared to the SAM method, the winter wheat planting area with the new method is closer to the reference

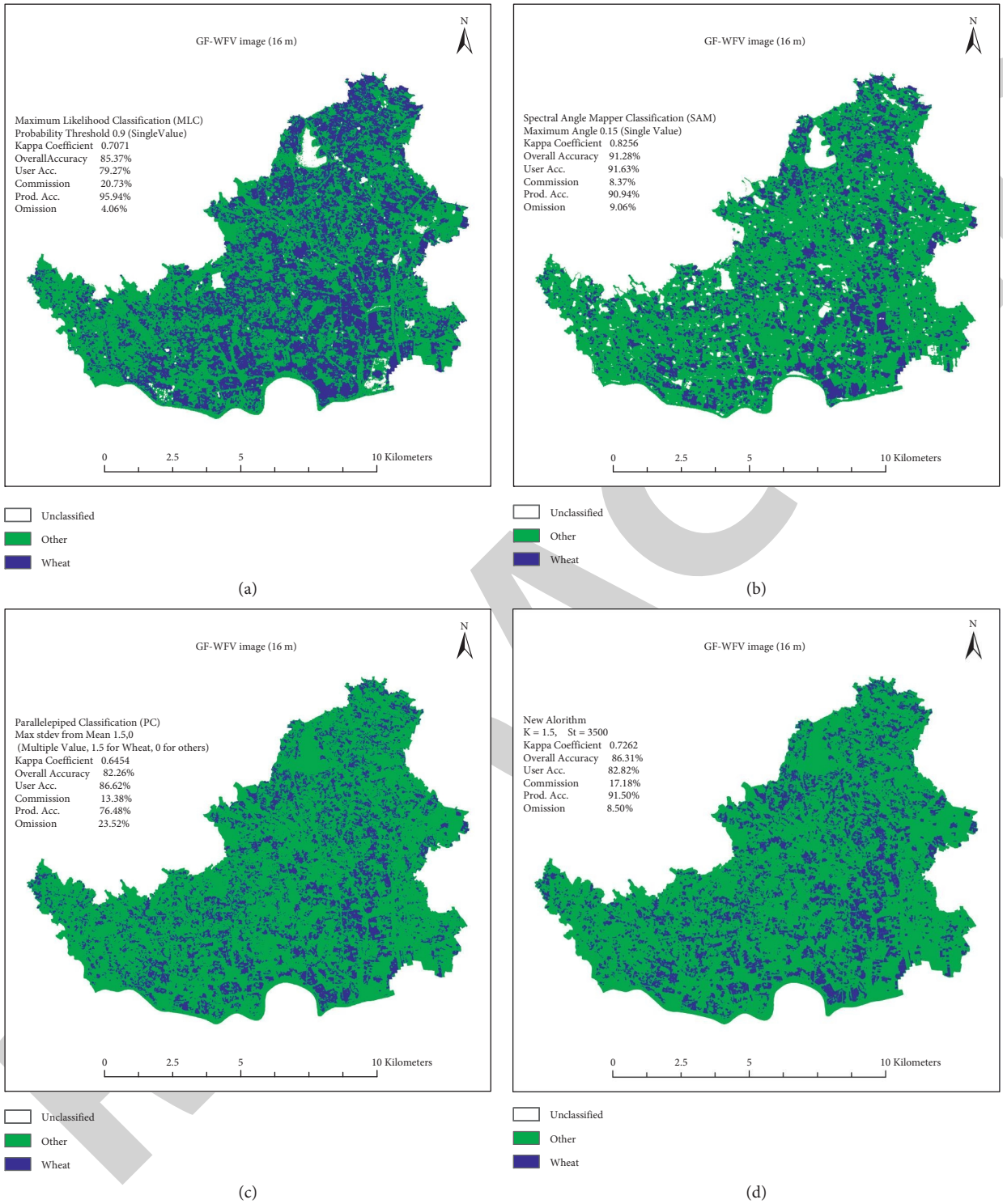

Figure 8: Best classification results on GF-WFV images in the study area from different methods. (a) MLC. (b) SAM. (c) PC. (d) New algorithm.

area. The SAM method has slightly higher accuracy on the GF-WFV image than the new algorithm, but compared to the new method, the winter wheat planting area with the SAM method (2257.02 hectares) is larger than the reference area.

Figures 7(c) and 7(d) demonstrate that (1) the classification results from the SAM method cannot match the actual natural boundaries affected by the mixed pixels leading to the overidentification and omission of winter wheat, as shown in the locations within the red boxes marked 1; (2) the SAM method misclassifies the ROIs due to the phenomenon of different objects having the same spectrum, as shown in the locations within the red boxes

Table 6: Classification results of 4 methods with 10 parameters in the study area.

Images	Methods	Parameters	Area of winter wheat (hectares)	Kappa	Classification accuracy				
					Overall accuracy (%)	User's accuracy (%)	Commission errors (%)	Producer's accuracy (%)	Omission errors (%)
GF-PMS (8 m)	MLC	0.8	3063.69	0.8337	91.67	87.74	12.26	96.28	3.72
		0.9	3063.60	0.8337	91.67	87.74	12.26	96.28	3.72
	SAM	0.1	1378.51	0.8559	92.82	97.82	2.18	87.16	12.84
		0.15	1812.13	0.8985	94.93	96.15	3.85	93.30	6.70
	PC	1.5	416.01	0.6316	81.79	99.90	0.10	62.54	37.46
		2	134.70	0.2636	63.98	99.91	0.09	25.83	74.17
		1.5, 0	1194.73	0.7951	89.82	98.24	1.76	80.46	19.54
		2, 0	2406.76	0.7975	89.89	89.67	10.33	89.47	10.53
	New algorithm	1.5	1018.77	0.9279	96.41	99.16	0.84	93.39	6.61
		2	2014.61	0.8028	90.16	91.22	8.78	88.28	11.72
GF-WFV (16 m)	MLC	0.8	4015.56	0.7071	85.37	79.27	20.73	95.94	4.06
		0.9	4015.56	0.7071	85.37	79.27	20.73	95.94	4.06
	SAM	0.1	2243.74	0.8058	90.29	91.46	8.54	88.97	11.03
		0.15	2257.02	0.8256	91.28	91.63	8.37	90.94	9.06
	PC	1.5	305.64	0.2047	60.11	95.09	4.91	21.65	78.35
		2	99.58	0.0434	51.99	96.06	3.94	4.55	95.45
		1.5, 0	2256.72	0.6454	82.26	86.62	13.38	76.48	23.52
		2, 0	4523.14	0.5095	75.51	68.86	31.14	93.48	6.52
	New algorithm	1.5	1975.18	0.7262	86.31	82.82	17.18	91.50	8.50
		2	3637.73	0.4550	72.71	64.88	35.12	98.62	1.38

marked 2; and (3) its classification results have the problem of salt-and-pepper noise, as shown in the locations within the red boxes marked 3.

4.1.3. Accuracy Analysis of the New Algorithm under Different Spatial Resolutions. From Table 6, we can find that the new method has the best accuracy on the GF-PMS image with 8 m spatial resolution with a K of 1.5. It has high and balanced user's and producer's accuracy, but low omission and commission error. The performance of the new method on the GF-WFV image with 16 m spatial resolution is average, and the kappa coefficient and overall accuracy are even worse than those of the spectral angle mapper classification method. This is consistent with the analysis from Table 3, because 70.12% of the total number of ROIs with an area less than 1000 m^2 in the study area result in the occurrence of more mixed pixels, making the image resolution not match the overall distribution of the size of ROIs on the 16 m image. So, the new algorithm cannot exploit its advantages.

In this paper, the parallelepiped classification method is used to process homogeneous ROIs. Although this method is not suitable for pixel-based classification, it obtains good results in classifying ROIs as a whole, reflecting the superiority of the new algorithm. Whether using other classification methods, such as spectral angle mapper, to deal with homogeneous ROIs could further improve the accuracy is worth further study.

From Figure 7(d), we can see that, by detecting the homogeneity of ROIs, the new method can well control the mixing problem of a small amount of spectral variation at the boundaries and inside the ROIs to solve the problem of salt-and-pepper noise effectively. The new algorithm does not need to rely on the spatial information of remote sensing images and only uses the images to obtain spectral information of ROIs. This makes it possible to obtain high-precision classification results by using medium-resolution remote sensing images, and the classification results correspond well with ground reality, so they have high practical value. In reality, the vector boundaries of the ownership parcel data will not change greatly in a short period (such as 3–5 years), so continuous observation and comparison of the parcels or regions can be achieved by using the new method. The prerequisite is the high-precision geometric correction of remote sensing images.

4.1.4. Matching Degree Analysis between the Size of Parcels and Spatial Resolution of Remote Sensing Images. Combining Table 6 with Figures 7 and 8, we find that the accuracy of the new algorithm on the GF-PMS (8 m) and GF-WFV (16 m) images of the study area was completely different. It can always get high accuracy from high-spatial-resolution images, which is suitable for the other methods. However, different methods are sensitive to different spatial resolution. The SAM method shows a small difference in accuracy between the two images. The new algorithm has a relatively large difference in accuracy between images with different spatial resolution and needs to match the spatial resolution of remote sensing images with the size of ownership parcels. It is also worth studying whether the classification accuracy of the new algorithm can be greatly enhanced by further improving the spatial resolution of remote sensing images in scattered growing region with small ROIs.

4.2. Applicability Analysis. Food stability is the foundation of social stability and agricultural subsidies. At present, subsidies for agricultural planting are based on the area of farmers' contracted fields instead of actually measured crop planting areas in practice. This makes the direction of subsidies unclear and imprecise, which is contrary to the practice of encouraging farmers to grow grain. Because the target of subsidies is not precise enough, farmers' enthusiasm to grow grain decreases, leading to the tendency of nongrain farmland becoming more serious. Therefore, it is urgent to improve the precision of agricultural subsidies by exploring and obtaining precise crop planting areas of peasant households for every season.

The experimental results in this paper demonstrate that it is feasible to extract crop planting areas based on medium-resolution remote sensing images and ownership parcel vector data. Moreover, under the condition that the spatial resolution of remote sensing images matches the size of ROIs, the classification accuracy is high, and the results can be associated with the ownership of field contract operations, which is a research direction for the realization of precise subsidies for agricultural planting in the future.

4.3. Limits. The new algorithm was implemented on the secondary development platform of Envi 5.3 using the IDL language. The ownership parcel vector data has 71,869 parcels. The GF-PMS and GF-WFV images are composed of $2{,}027 \times 1{,}591$ and $1{,}014 \times 796$ grid cells, respectively. During the process of implementing the new algorithm, it was necessary to use the parcel data to segment the raster image logically and to detect the homogeneity of each ROI corresponding to each parcel.

Due to a large amount of data, the computational efficiency is lower than that of other comparison methods on a desktop computer with an i7-7600 CPU, 16 GB RAM, and Microsoft Windows 10 using the 64-bit option. At present, the proposed algorithm is implemented on a single-core CPU and has the characteristics of large amounts of data, low coupling, and high computational density, which is suitable to be parallelized. Its computational efficiency can be improved by parallel computing, such as MPI, OpenMP, cloud computing, and Compute Unified Device Architecture (CUDA). Therefore, parallelization of the proposed algorithm based on parallel computing is also worth further research.

5. Conclusions

This paper proposed a new algorithm for extracting winter wheat planting areas based on ownership parcel vector data and medium-resolution remote sensing images to enhance the winter wheat classification accuracy in complex planting areas. First, the region of interest (ROI) of each parcel was generated by using the parcel data to segment the image. Then, the homogeneity of each ROI was detected by its statistical indices (mean value and standard deviation), calculated from the spectral information of the image to get homogeneous and nonhomogeneous ROIs. The parallelepiped classifier and rule-based feature extraction classification methods were utilized to extract winter wheat planting areas from homogeneous and nonhomogeneous ROIs, respectively. Finally, in order to achieve the final classification result, the two classification results were combined.

The experiments verified that the new algorithm could extract the winter wheat planting areas by combining a GF-PMS image with 8 m spatial resolution and the ownership parcels (71869 parcels) in a complex planting area of 103.60 km^2 in central China, which covers the 19 administrative villages of Fengle Town, in Feixi County, Hefei City, Anhui Province, China. The kappa coefficient and overall accuracy of the new algorithm reached 0.9279 and 96.41%, respectively. The new algorithm can effectively control the mixing of a few spectral variations within the boundary and interior of parcel and solve the problem of salt-and-pepper noise. It does not rely on the use of remote sensing images to extract spatial location information and only uses images for the spectral information of ROIs, which makes the classification results have high accuracy with remote sensing images with medium spatial resolution. It has high user's and producer's accuracy, which were higher than those of maximum likelihood, spectral angle mapper, and parallelepiped classification methods.

The new algorithm needs to match the spatial resolution of the image with the size of the ROIs to ensure that each ROI has a majority of pure pixels but not mixed pixels. If they do not match, the advantages of the proposed classification algorithm cannot be realized, and the accuracy of the classification results is worse than that with the traditional pixel-based classification methods. A GF-WFV image with 16 m spatial resolution was utilized in the scattered growing region with small parcels; thus, it requires high-precision geometric correction of remote sensing images.

In this study, a parallelepiped classification was utilized to process the homogeneous ROIs. Whether other classification methods can further improve the accuracy of the new method deserves further study. It is also worth studying whether the classification accuracy of the new algorithm can be greatly enhanced by further improving the spatial resolution of images in scattered growing regions with small parcels. Research could also focus on inserting parallel computing into the new algorithm to improve its computational efficiency.

Data Availability

The satellite image with 8 m spatial resolution from Gaofen-1 carrying a panchromatic multispectral sensor (PMS) and the satellite image with 16 m spatial resolution from GF1 carrying a wide field view (WFV) were downloaded from http://36.112.130.153:7777/DSSPlatform/index.html. The ownership parcel vector data are confidential.

Conflicts of Interest

The authors declare no conflicts of interest.

Acknowledgments

The authors thank the Agriculture and Rural Bureau of Feixi County, Anhui Province, China, for data support. This research was funded by the Natural Science Research Project of University in Anhui Province (grant nos. KJ2018A0509 and KJ2019A0763) and the Natural Science Foundation of Anhui Province (2108085QD151).

References

[1] N.-T. Son, C.-F. Chen, C.-R. Chen, and H.-Y. Guo, "Classification of multitemporal sentinel-2 data for field-level monitoring of rice cropping practices in taiwan," *Advances in Space Research*, vol. 65, no. 8, pp. 1910–1921, 2020.

[2] L. Xun, P. Wang, and L. Li, "Identifying crop planting areas using fourier-transformed feature of time series MODIS leaf area index and sparse-representation-based classification in the north China plain," *International Journal of Remote Sensing*, vol. 40, no. 5–6, pp. 2034–2052, 2019.

[3] J. Zhang, X. Li, and Y. Wu, "Object oriented estimation of winter wheat planting area using remote sensing data," *Transactions of the Chinese Society of Agricultural Engineering*, vol. 24, no. 5, pp. 156–160, 2008.

[4] J. Schmedtmann and M. Campagnolo, "Making the use of remote sensing for agricultural subsidy control more effective: automatizing photo interpretation of Satellite Imagery over Southern Portugal in the Context of the European CAP," in *Proceedings of the AGU Fall Meeting, Session: Earth Observations for National to Global Agricultural and Rangeland Monitoring (GEOGLAM)*, San Francisco, CA, USA, 2014.

[5] M. K. Gumma, P. S. Thenkabail, K. C. Deevi et al., "Mapping cropland fallow areas in Myanmar to scale up sustainable intensification of pulse crops in the farming system," *GIScience and Remote Sensing*, vol. 55, no. 6, pp. 926–949, 2018.

[6] Y. Guo, H. Xia, and L. Pan, "Development of a new phenology algorithm for fine mapping of cropping intensity in complex planting areas using sentinel-2 and google earth engine," *ISPRS International Journal of Geo-Information*, vol. 10, no. 587, 2021.

[7] P. Teluguntla, D. Ryu, B. George, J. Walker, and H. Malano, "Mapping flooded rice paddies using time series of MODIS imagery in the krishna river basin, India," *Remote Sensing*, vol. 7, no. 7, pp. 8858–8882, 2015.

[8] W. Li, D. Fu, and F. Su, "Spatial-temporal evolution and analysis of the driving force of oil palm patterns in Malaysia from 2000 to 2018," *ISPRS International Journal of Geo-Information*, vol. 9280 pages, 2020.

[9] S. Wu, H. Lu, and H. Guan, "Optimal bands combination selection for extracting garlic planting area with multi-temporal sentinel-2 imagery," *Sensors*, vol. 21, no. 5556, 2021.

[10] A. Nasrallah, N. Baghdadi, and M. Mhawej, "A novel approach for mapping wheat areas using high resolution sentinel-2 images," *Sensors*, vol. 18, no. 2089, 2018.

[11] P. Teluguntla, P. S. Thenkabail, A. Oliphant et al., "A 30-m landsat-derived cropland extent product of Australia and China using random forest machine learning algorithm on google earth engine cloud computing platform," *ISPRS Journal of Photogrammetry and Remote Sensing*, vol. 144, pp. 325–340, 2018.

[12] M. H. Asad and A. Bais, "Weed detection in canola fields using maximum likelihood classification and deep convolutional neural network," *Information Processing in Agriculture*, vol. 7, no. 4, pp. 535–545, 2020.

[13] A. Ozdarici-Ok, A. Ok, and K. Schindler, "Mapping of agricultural crops from single high-resolution multispectral images-data-driven smoothing vs. Parcel-based smoothing," *Remote Sensing*, vol. 7, no. 5, pp. 5611–5638, 2015.

[14] A. Moiane and A. M. L. Machado, "Class-based affinity propagation for hyperspectral image dimensionality reduction and improvement of maximum likelihood classification accuracy," *Bulletin of Geodetic Sciences*, vol. 25, no. 1, Article ID e2019004, 2019.

[15] O. B. Özdemir and Y. Y. Çetin, *Improved Hyperspectral Vegetation Detection Using Neural Networks with Spectral Angle Mapper*, San Francisco, CA, USA, 2017.

[16] G. Randazzo, M. Cascio, and M. Fontana, "Mapping of Sicilian pocket beaches land use/land cover with sentinel-2 imagery: a case study of messina Province," *Land*, vol. 10678 pages, 2021.

[17] K. Tatsumi, Y. Yamashiki, and C. L. R. Taipe, "Crop classification of upland fields using random forest of time-series landsat 7 ETM+ data," *Computers and Electronics in Agriculture*, vol. 115, pp. 171–179, 2015.

[18] J. Wang, Y. Zhao, C. Li, L. Yu, D. Liu, and P. Gong, "Mapping global land cover in 2001 and 2010 with spatial-temporal consistency at 250m resolution," *ISPRS Journal of Photogrammetry and Remote Sensing*, vol. 103, pp. 38–47, 2015.

[19] F. Zhang and X. Yang, "Improving land cover classification in an urbanized coastal area by random forests: the role of variable selection," *Remote Sensing of Environment*, vol. 251112105 pages, 2020.

[20] L. Loosvelt, J. Peters, H. Skriver, B. De Baets, and N. E. C. Verhoest, "Impact of reducing polarimetric SAR input on the uncertainty of crop classifications based on the random forests algorithm," *IEEE Transactions on Geoscience and Remote Sensing*, vol. 50, no. 10, pp. 4185–4200, 2012.

[21] G. Mountrakis, J. Im, and C. Ogole, "Support vector machines in remote sensing: a review," *ISPRS Journal of Photogrammetry and Remote Sensing*, vol. 66, no. 6, pp. 247–259, 2011.

[22] J. M. Guerrero, G. Pajares, M. Montalvo, J. Romeo, and M. Guijarro, "Support vector machines for crop/weeds identification in maize fields," *Expert Systems with Applications*, vol. 39, no. 12, pp. 11149–11155, 2012.

[23] F. Camacho de Coca, B. Fuster, and W. Li, "Crop specific algorithms trained over ground measurements provide the best performance for GAI and FAPAR estimates from landsat-8 observations," *Remote Sensing of Environment*, vol. 260112453 pages, 2021.

[24] G. Tana, H. Letu, Z. Cheng, and R. Tateishi, "Wetlands mapping in north America by decision rule classification using MODIS and ancillary data," *IEEE Journal of Selected Topics in Applied Earth Observations and Remote Sensing*, vol. 6, no. 6, pp. 2391–2401, 2013.

[25] W. B. Cohen and S. N. Goward, "Landsat's role in ecological applications of remote sensing," *BioScience*, vol. 54, no. 6, pp. 535–545, 2004.

[26] M. Ozdogan and G. Gutman, "A new methodology to map irrigated areas using multi-temporal MODIS and ancillary data: an application example in the continental US," *Remote Sensing of Environment*, vol. 112, no. 9, pp. 3520–3537, 2008.

[27] A. Asgarian, A. Soffianian, and S. Pourmanafi, "Crop type mapping in a highly fragmented and heterogeneous agricultural landscape: a case of Central Iran using multi-temporal landsat 8 imagery," *Computers and Electronics in Agriculture*, vol. 127, pp. 531–540, 2016.

[28] Z. Pan, J. Huang, Q. Zhou et al., "Mapping crop phenology using NDVI time-series derived from HJ-1 A/B data,"

International Journal of Applied Earth Observation and Geoinformation, vol. 34, pp. 188–197, 2015.

[29] L. Zhong, L. Hu, L. Yu, P. Gong, and G. S. Biging, "Automated mapping of soybean and corn using phenology," *ISPRS Journal of Photogrammetry and Remote Sensing*, vol. 119, pp. 151–164, 2016.

[30] L. G. J. Van Bussel, E. Stehfest, S. Siebert, C. Müller, and F. Ewert, "Simulation of the phenological development of wheat and maize at the global scale," *Global Ecology and Biogeography*, vol. 24, no. 9, pp. 1018–1029, 2015.

[31] D. C. Duro, S. E. Franklin, and M. G. Dubé, "A comparison of pixel-based and object-based image analysis with selected machine learning algorithms for the classification of agricultural landscapes using SPOT-5 HRG imagery," *Remote Sensing of Environment*, vol. 118, pp. 259–272, 2012.

[32] X. E. Pantazi, D. Moshou, T. Alexandridis, R. L. Whetton, and A. M. Mouazen, "Wheat yield prediction using machine learning and advanced sensing techniques," *Computers and Electronics in Agriculture*, vol. 121, pp. 57–65, 2016.

[33] D. Paudel, H. Boogaard, and A. de Wit, "Machine learning for large-scale crop yield forecasting," *Agricultural Systems*, vol. 187, no. 103016, 2021.

[34] J. Peña, P. Gutiérrez, and C. Hervás-Martínez, "Object-based image classification of summer crops with machine learning methods," *Remote Sensing*, vol. 6, pp. 5019–5041, 2014.

[35] J. C. Tilton, Y. Tarabalka, P. M. Montesano, and E. Gofman, "Best merge region-growing segmentation with integrated nonadjacent region object aggregation," *IEEE Transactions on Geoscience and Remote Sensing*, vol. 50, no. 11, pp. 4454–4467, 2012.

[36] M. Chellasamy, R. T. Zielinski, and M. H. Greve, "A multievidence approach for crop discrimination using multitemporal WorldView-2 imagery," *IEEE Journal of Selected Topics in Applied Earth Observations and Remote Sensing*, vol. 7, no. 8, pp. 3491–3501, 2014.

[37] Y. Kang and L. Zhou, "RubE: rule-based methods for extracting product features from online consumer reviews," *Information & Management*, vol. 54, no. 2, pp. 166–176, 2017.

[38] J. Xiong, P. Thenkabail, and J. Tilton, "Nominal 30-m cropland extent map of continental africa by integrating pixel-based and object-based algorithms using sentinel-2 and landsat-8 data on google earth engine," *Remote Sensing*, vol. 91065 pages, 2017.

[39] G. Chen, J.-C. Thill, S. Anantsuksomsri, N. Tontisirin, and R. Tao, "Stand age estimation of rubber (hevea brasiliensis) plantations using an integrated pixel- and object-based tree growth model and annual landsat time series," *ISPRS Journal of Photogrammetry and Remote Sensing*, vol. 144, pp. 94–104, 2018.

[40] T. Zhou, J. Pan, P. Zhang, S Wei, and T Han, "Mapping winter wheat with multi-temporal SAR and optical images in an urban agricultural region," *Sensors*, vol. 171210 pages, 2017.

[41] A. I. De Castro, J. Six, and R. E. Plant, "Mapping crop calendar events and phenology-related metrics at the parcel level by object-based image analysis (OBIA) of MODIS-NDVI time-series: a case study in central California," *Remote Sensing*, vol. 101745 pages, 2018.

[42] J. Huang, H. Wang, Q. Dai, and D. Han, "Analysis of NDVI data for crop identification and yield estimation," *IEEE Journal of Selected Topics in Applied Earth Observations and Remote Sensing*, vol. 7, no. 11, pp. 4374–4384, 2014.

[43] P. Li, C. Xiao, and Z. Feng, "Mapping rice planted area using a new normalized EVI and SAVI (NVI) derived from landsat-8 OLI," *IEEE Geoscience and Remote Sensing Letters*, vol. 15, no. 12, pp. 1822–1826, 2018.

[44] M. Wei, B. Qiao, J. Zhao, and X. Zuo, "The area extraction of winter wheat in mixed planting area based on sentinel-2 a remote sensing satellite images," *International Journal of Parallel, Emergent and Distributed Systems*, vol. 35, no. 3, pp. 297–308, 2020.

[45] R. D'Andrimont, G. Lemoine, and M. Van der Velde, "Targeted grassland monitoring at parcel level using sentinels, street-level images and field observations," *Remote Sensing*, vol. 101300 pages, 2018.

[46] M. J. Falkowski and J. A. Manning, "Parcel-based classification of agricultural crops via multitemporal landsat imagery for monitoring habitat availability of western burrowing owls in the imperial valley agro-ecosystem," *Canadian Journal of Remote Sensing*, vol. 36, no. 8, pp. 750–762, 2010.

[47] M. Ebadian, M. E. Shedden, E. Webb et al., "Impact of parcel size, field shape, crop yield, storage location, and collection equipment on the performance of single-pass cut-and-chip harvest system in commercial shrub willow fields," *Bioenergy Research*, vol. 11, no. 2, pp. 364–381, 2018.

[48] J. C. Foltête, "A parcel-based graph to match connectivity analysis with field action in agricultural landscapes: is node removal a reliable method," *Landscape and Urban Planning*, vol. 178, pp. 32–42, 2018.

[49] P. Zhang, S. Hu, W. Li, and C. Zhang, "Parcel-level mapping of crops in a smallholder agricultural area: a case of Central China using single-temporal VHSR imagery," *Computers and Electronics in Agriculture*, vol. 175, Article ID 105581, 2020.

[50] E. Derenyi, "A small crop information system," *Proceedings of Remote Sensing for Natural Resources*, vol. 1, pp. 78–87, 1979.

[51] F. Levavasseur, P. Martin, C. Bouty et al., "RPG Explorer: a new tool to ease the analysis of agricultural landscape dynamics with the Land Parcel Identification System," *Computers and Electronics in Agriculture*, vol. 127, pp. 541–552, 2016.

[52] L. Deng, Z. Shen, and Y. Ke, "Winter wheat planting area extraction using multi-temporal remote sensing images based on field parcel," *Transactions of the Chinese Society of Agricultural Engineering*, vol. 34, no. 21, pp. 157–164, 2018.

[53] C. Zhu, J. Luo, and Z. Shen, "Winter wheat planting area extraction using multi-temporal remote sensing data based on field parcel characteristic," *Transactions of the Chinese Society of Agricultural Engineering*, vol. 27, no. 9, pp. 94–99, 2011.

[54] Q. Huang, Z. Zeng, and G. Xie, "Investigation on crop planting structure based on synergy of high spatial-temporal resolution remote sensing data," *Journal of Southern Agriculture*, vol. 48, no. 3, pp. 552–560, 2017.

[55] Y. Sun, J. Luo, L. Xia et al., "Geo-parcel-based crop classification in very-high-resolution images via hierarchical perception," *International Journal of Remote Sensing*, vol. 41, no. 4, pp. 1603–1624, 2020.

[56] X. Gu, Y. Pan, and X. He, "Measurement of sown area of winter wheat based on per-field classification and remote sensing imagery," *Chineise Journal of Remote Sensing*, vol. 14, no. 4, pp. 789–805, 2010.

[57] F. Löw and G. Duveiller, "Determining suitable image resolutions for accurate supervised crop classification using remote sensing data," *SPIE, Remote Sensing, Earth Resources & Environmental Remote Sensing/gis Applications IV*, vol. 8893, 2013.

[58] M. Fauvel, J. A. Palmason, and J. A. A. Benediktsson, "Classification of remote sensing imagery with high spatial

resolution," *Proceedings, Image and Signal Processing for Remote Sensing XI*, vol. 5982, Article ID 598201, 2005.

[59] N. Koutsias, M. Pleniou, G. Mallinis, F. Nioti, and N. I. Sifakis, "A rule-based semi-automatic method to map burned areas: exploring the USGS historical landsat archives to reconstruct recent fire history," *International Journal of Remote Sensing*, vol. 34, no. 20, pp. 7049–7068, 2013.

[60] A. R. Phalke, M. Özdoğan, P. S. Thenkabail et al., "Mapping croplands of europe, Middle East, Russia, and central asia using landsat, random forest, and google earth engine," *ISPRS Journal of Photogrammetry and Remote Sensing*, vol. 167, pp. 104–122, 2020.